Energy dissipation in soil samples during cyclic triaxial simulations

Energy dissipation in soil samples during cyclic triaxial simulations

Joel Keishing[1], Xin Huang[2,3] and Kevin J. Hanley[1*]

[1] School of Engineering, Institute for Infrastructure and Environment, The University of Edinburgh, Edinburgh EH9 3JL, United Kingdom

[2] Key Laboratory of Geotechnical and Underground Engineering, Ministry of Education, Tongji University, 1239 Siping Road, Shanghai 200092, China

[3] Department of Geotechnical Engineering, Tongji University, 1239 Siping Road, Shanghai 200092, China

Abstract

Energy terms were computed in a set of undrained cyclic triaxial discrete-element method simulations which form a parametric study of five factors: void ratio, initial mean effective stress, mean deviator stress, deviator stress amplitude and compressive/extensive initial loading. Void ratio is the only one of these factors which significantly affects the relationship between the excess pore water pressure and the unit energy dissipated (energy dissipated per unit volume). The trends in both the number of complete cycles and the unit energy up to the onset of liquefaction match experimental data. Through analysis of the micro-scale particle and contact information, a preferred contact orientation for frictional dissipation of 30–40° was found. Following a shear reversal, there is a period of negligible frictional dissipation in these simulations of around 0.04% axial strain. This explains, from an energy perspective, why many load cycles are needed to induce liquefaction if their amplitude is very small. A commonly used energy-based model to evaluate the liquefaction potential of a soil was assessed. A substantial improvement in the predictive ability of this model may be achieved by including the mean deviator stress.

Keywords: Friction; Discrete element modelling; Particle-scale behaviour; Numerical modelling; Sands; Anisotropy

[*] Corresponding author. E-mail: k.hanley@ed.ac.uk; Phone: +44 (0)13 1650 5712; Fax: +44 (0)13 1650 6554

1 Introduction

Energy is a key consideration when evaluating the response of soil subjected to cyclic loading. The damping ratio is routinely calculated using the areas on a stress–strain plot underneath and enclosed by a hysteresis loop, e.g., [1, 2]. Numerous energy-based methods for liquefaction assessment have been proposed [3-9]. Liang et al. [10] describe the advantages of energy-based methods for liquefaction assessment compared to the stress- or strain-based methods respectively developed by Seed & Idriss [11] and Dobry et al. [12].

The damping ratio and models for liquefaction assessment apply to an entire soil sample. They do not give any insight into the motions and interactions of individual soil grains which cause the storage of elastic energy and dissipation of energy measurable at the macro-scale. This limitation is difficult to overcome in physical experiments. However, all of the information needed to compute the kinetic energy of each grain, the strain energy at each interparticle contact and the energy dissipated during each grain–grain interaction can be obtained from discrete-element method (DEM) simulations with high accuracy. Hanley et al. [13] quantified the energy dissipated by frictional sliding of particles during drained triaxial compression. They demonstrated that the frictional dissipation and boundary work were almost equal, found the existence of a preferential orientation for frictional dissipation in triaxial shearing, and recommended the use of a thermodynamically consistent work equation in constitutive modelling of dense sands. This built upon prior monotonic simulation studies which tracked energy dissipation [14-18].

DEM has also been applied to track energy terms during cyclic loading of soil. El Shamy & Denissen [19] plotted the time histories of individual energy components up to liquefaction, varying the loading conditions applied in the simulations. A follow-up parametric study [20] varied the sample porosity, maximum strain amplitude and cycle frequency while individual energy terms (boundary work, frictional dissipation, damping, strain and kinetic) were tracked. Zamani & El Shamy [21] computed the dissipated energy for a range of soil–foundation–structure systems. Tong & Wang [22] showed the effect of the number of particles, particle aspect ratio and aging (captured by contact creep) on the energy terms per unit volume for cyclic shearing. In these prior studies, the energy data, though

computed using micro-scale particle and contact information, have been interpreted at a macro-scale: the important variations in energy that occur within an individual load cycle have not been considered, e.g., the changes that occur upon shear reversal from compression to extension or *vice versa*. This is one key difference between this and prior studies, and is a major novelty of this paper.

This paper initially presents a comprehensive parametric study in which the void ratio, initial mean effective stress, mean deviator stress, deviator stress amplitude and compressive/extensive initial loading are systematically varied in a set of undrained cyclic loading simulations. The trends in each parameter are compared with experimental data; this paper is the first DEM study which achieves good qualitative agreement with physical experiments across this broad range of parameters.

The frictional dissipation, boundary work and strain energy are compared between cycles to show variations from the start of shearing up to the onset of liquefaction. In addition, the significant variations in frictional dissipation during an individual cycle, e.g., changes upon shear reversal, are studied in detail. For the first time, the relationship between the accumulated pore water pressure and the dissipated energy per unit volume, a relationship about which there is some uncertainty based on laboratory test data, is explored in this idealised numerical environment. Finally, the applicability of a commonly used energy-based method to evaluate the liquefaction potential of a soil [5] is assessed, and a novel recommendation is made to improve its predictive ability for samples with initial stress anisotropy.

2 DEM Simulations

Cuboidal samples were created which contained 28,309 unbreakable, spherical particles. The grading used, shown in Fig. 1, was not representative of any specific sand; particle diameters spanned the range 0.1–1 mm (D_{50} = 0.516 mm), with C_u = 3.004 and C_c = 0.573 indicating a poorly graded sand. It is noted that the results and conclusions presented in this paper are based on this single grading; while their applicability to other gradings is highly likely, further simulations would be required to prove this definitively.

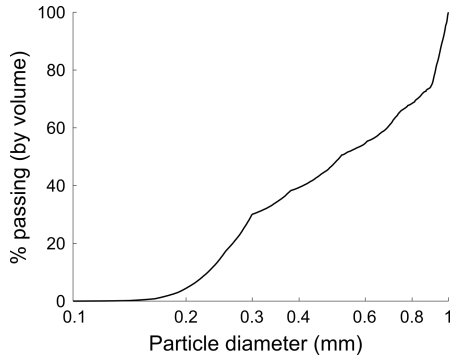

Fig. 1: Particle size distribution of the numerical samples

Periodic boundary conditions were chosen to ensure homogeneous samples [23]. The sample preparation approach described by Hanley et al. [24] was adopted. Firstly, particles were sequentially placed within a periodic cell, without contacting any existing particles, at positions chosen at random. Then the periodic boundaries were moved closer together using a servo controller until a stable, equilibrated sample had been achieved at the desired stress state. Stresses were computed from the contact forces [25]. Three different interparticle friction coefficients (μ = 0.15, 0.175 and 0.2) were used during sample preparation to control the void ratio, e. Five different combinations of effective continuum normal stress were attained (σ_x', σ_y' and σ_z' with respect to conventional Cartesian axes).

After sample preparation, μ was increased to 0.25 [26] and cyclic shearing commenced under stress control as illustrated in Fig. 2. The sample volume was maintained constant to capture undrained shearing while the deviator stress, $q = \sigma_z' - \frac{1}{2}\left(\sigma_x' + \sigma_y'\right)$, was varied according to

$$q = q_{mean} \pm q_{cyc} \sin\left(\frac{2\pi t}{T}\right). \quad (1)$$

q_{mean} is the mean deviator stress, q_{cyc} is the deviator stress amplitude, T is the cycle period and t is time. The '+' case in Eq. (1) corresponds to initial compressive loading (IC); the '−' case to initial extensive loading (IE). The servo-control algorithm maintained $\sigma_x' = \sigma_y'$ during shearing, resulting in strains in the *x* and *y* directions which were almost equal.

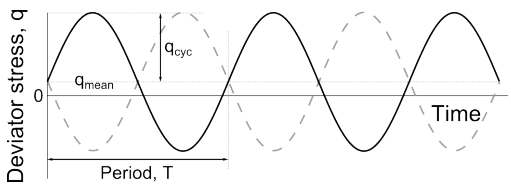

Fig. 2: Schematic of two stress-controlled cyclic simulations with mean deviator stress q_{mean}, deviator stress amplitude q_{cyc} and period T. The solid black line shows initial compression; the dashed grey line shows initial extension

T was fixed at 0.25 s for all simulations, i.e., loading frequency of 4 Hz. The frequency was not varied as many studies (although not all: [27]) have found that frequency has little effect on energy dissipation and the stress–strain response, e.g., [20, 28]. This frequency ensured quasi-static conditions: inertia numbers were less than the 7.9 x 10^{-5} threshold identified by Lopera Perez et al. [29] throughout shearing, except immediately before the onset of liquefaction in cases where the mean effective stress p' approaches zero. For this paper, the onset of liquefaction was defined as either $p' \approx 0$ or an axial strain of $\pm$ 5% in the z direction. This is the criterion that is typically used in laboratory tests for identifying initial liquefaction and assessing liquefaction potential, e.g., [30, 31].

Table 1 shows the parameters for the ten simulations run. S1 is the 'base case' with e = 0.4534, p'_0 = 300 kPa, q_{mean} = 0 kPa, q_{cyc} = 80 kPa and initial compression. Individual parameters were varied from these values. For S2 and S3, e was varied while the other parameters were fixed; p'_0 was varied for S4 and S5; q_{mean} for S6 and S7; q_{cyc} for S8 and S9; initial extensive loading conditions for S10. For S4–S7, the changes in p'_0 and q_{mean} also had some effect on e. This is discussed when the results are presented.

Table 1. Void ratios, initial mean effective stresses, mean deviator stresses, deviator stress amplitudes and IC/IE loading conditions for the ten simulations. S1 is the 'base case'; a bold font is used to identify the primary changes from this base case for the other nine simulations

Simulation ID	Void ratio, e	Initial mean effective stress, p_0' (kPa)	Mean deviator stress, q_{mean} (kPa)	Deviator stress amplitude, q_{cyc} (kPa)	Initial compression (IC) / extension (IE)
S1	0.4534	300	0	80	IC
S2	**0.4470**	300	0	80	IC
S3	**0.4586**	300	0	80	IC
S4	0.4516	**350**	0	80	IC
S5	0.4598	**150**	0	80	IC
S6	0.4529	300	**45**	80	IC
S7	0.4513	300	**90**	80	IC
S8	0.4534	300	0	**60**	IC
S9	0.4534	300	0	**100**	IC
S10	0.4534	300	0	80	**IE**

These simulations were run using a version of the open-source LAMMPS code [32], adapted to include computations of stress and the various energy terms described in this paper. A simplified Hertz-Mindlin contact model was implemented and used for these simulations. The normal component of the contact force, $\boldsymbol{F}_n$, is given by Eq. (2):

$$\boldsymbol{F}_n = \frac{4Gr_g}{3(1-\upsilon)}\alpha_n^{\frac{3}{2}}\boldsymbol{n} \tag{2}$$

α_n is the overlap between elastic spheres a and b, G is the particle shear modulus, υ is the particle Poisson's ratio, $r_g = \sqrt{\frac{r_a r_b}{r_a + r_b}}$ with particle radii r_a and r_b, and $\boldsymbol{n}$ is a unit vector along the line

connecting the sphere centres. The shear or tangential component of the contact force, $\boldsymbol{F}_t$, is incrementally calculated using Eq. (3) and (4):

$$\boldsymbol{F}_t^{\beta} = \boldsymbol{F}_t^{\beta-1} - k_t \delta \boldsymbol{\alpha}_t \tag{3}$$

$$k_t = \frac{4Gr_g}{2-\upsilon}\sqrt{\alpha_n} \tag{4}$$

k_t is the contact shear tangent stiffness, $\beta - 1$ and β represent consecutive time-steps and $\delta\boldsymbol{\alpha}_t$ is the increment of relative tangential displacement during time-step β.

It has sometimes been recommended to rescale the shear force before it is updated, i.e., rescale $\boldsymbol{F}_t^{\beta-1}$, whenever the normal force decreases [33]. The argument is that a reduced contact area could no longer support the same shear force. However, this rescaling causes an overestimation of energy dissipation [34]. Appendix A quantifies the sizable error introduced into the energy balance for a single collision of two spheres. This rescaling was not adopted for the simulations presented in this paper as the analysis requires energy terms to be quantified accurately.

A Coulomb slip criterion is imposed to limit the tangential force:

$$|\boldsymbol{F}_t^{\beta}| \leq \mu|\boldsymbol{F}_n| \tag{5}$$

G was set at 1.46 GPa to obtain a more realistic stress–strain response in these constant-volume simulations than if a realistic G for quartz were adopted [35]. Using this shear modulus, the maximum overlap between any pair of particles in the system was 3.3% of the mean particle radius for the isotropic base case sample at p_0' = 300 kPa, while the mean overlap between particles was 0.6%. The particle density was 2650 kg/m^3 and υ = 0.2. Gravity and damping were both inactive during shearing.

3 Energy Calculations

Apart from allowing q to become negative, the other energy terms computed during these cyclic simulations are the same as those described in [13] and so a summary is given here. The increment of boundary work per unit volume is [36]:

$$\delta W = \sigma'_x \delta\varepsilon_x + \sigma'_y \delta\varepsilon_y + \sigma'_z \delta\varepsilon_z \tag{6}$$

The incremental normal strains, $\delta\varepsilon_x$, $\delta\varepsilon_y$, $\delta\varepsilon_z$, were determined from the movements of the periodic boundaries. In general, Eq. (6) can be decomposed into increments of distortional and volumetric work per unit volume [36]. For these constant-volume simulations, it was verified that δW matches the former (the product of q and increment of triaxial shear strain). In each time-step, β, Eq. (6) was multiplied by the current sample volume, V^β, and accumulated as the total boundary work:

$$W^\beta = W^{\beta-1} + \delta W^\beta V^\beta \tag{7}$$

The translational and rotational kinetic energies are calculated as

$$E_{kt} = \frac{1}{2}\sum_{i=1}^{N_p} m_i v_i^2 \tag{8}$$

$$E_{kr} = \frac{1}{2}\sum_{i=1}^{N_p} I_i \omega_i^2 \tag{9}$$

N_p is the number of particles in the simulation, m_i, v_i and ω_i are the respective mass, translational speed and rotational speed of particle i, and $I_i = 0.4 m_i r_i^2$ is the moment of inertia of a spherical particle i of radius r_i.

If sliding occurs at contact j during time-step β, according to the criterion given by Eq. (5), then the accumulated energy dissipated by friction at the contact is

$$E_{f\_j}^\beta = E_{f\_j}^{\beta-1} + \delta E_{f\_j}^\beta \tag{10}$$

$$\delta E_{f\_j}^\beta = \frac{\left|\boldsymbol{F}_t^{\beta-1} + \boldsymbol{F}_t^\beta\right|}{2} \frac{\left|\boldsymbol{F}_{t\_o}^\beta - \boldsymbol{F}_t^\beta\right|}{k_t} \tag{11}$$

where $\boldsymbol{F}_{t\_o}^{\beta}$ is the tangential force computed using Eq. (3) before the Coulomb slip criterion has been applied. The normal component of strain energy for a single Hertzian contact, j, is given by [13]:

$$E_{sn\_j} = \frac{2}{5}|\boldsymbol{F}_n|\alpha_n \tag{12}$$

The tangential component is calculated incrementally after the slip criterion has been applied, if necessary. At contact j,

$$E_{st\_j}^{\beta} = E_{st\_j}^{\beta-1} + \delta E_{st\_j}^{\beta} \tag{13}$$

$$\delta E_{st\_j}^{\beta} = \frac{\left|\boldsymbol{F}_t^{\beta-1} + \boldsymbol{F}_t^{\beta}\right|}{2}\frac{\left|\boldsymbol{F}_t^{\beta} - \boldsymbol{F}_t^{\beta-1}\right|}{k_t} \tag{14}$$

The total frictional dissipation and the normal and tangential components of strain energy at time-step β are found by summation over all N_c contacts:

$$E_{sn} = \sum_{j=i}^{N_c} E_{sn\_j} \tag{15}$$

$$E_{st}^{\beta} = E_{st}^{\beta-1} + \sum_{j=i}^{N_c} \delta E_{st\_j}^{\beta} \tag{16}$$

$$E_{f}^{\beta} = E_{f}^{\beta-1} + \sum_{j=i}^{N_c} \delta E_{f\_j}^{\beta} \tag{17}$$

The strain energy may be converted to other forms of energy whereas frictional sliding is purely dissipative. Finally, the error in the energy balance, ΔE, was computed as

$$\Delta E = W^{\beta} - E_f^{\beta} + E_{sn}^0 + E_{st}^0 + E_{kt}^0 + E_{kr}^0 - E_{sn}^{\beta} - E_{st}^{\beta} - E_{kt}^{\beta} - E_{kr}^{\beta} \tag{18}$$

where the '0' and β superscripts respectively indicate the value of that energy term at the start of shearing or at some subsequent time-step. The error for each simulation was negligible, confirming (i) the energy terms were computed correctly in the code, and (ii) there was no spurious generation of energy indicating a numerical instability.

4 Results and Discussion

4.1 Base case (S1)

Fig. 3(a) shows the stress–strain behaviour for S1 with a 'positive compression' sign convention. p' decreases from its initial value of 300 kPa to 35 kPa at the onset of liquefaction (at 5% axial strain in this case). The corresponding energy terms are shown in Fig. 3(b). The accumulated energy dissipated by friction increases monotonically as expected, although with a noticeable nonlinearity: upon shear reversal, there is a brief period during which negligible frictional dissipation occurs. This is discussed in more detail along with Fig. 9. The normal component of strain energy decreases with each cycle in line with the mean effective stress. The shear component, which is more than one order of magnitude smaller than the normal strain energy, similarly decreases with each cycle. The non-monotonic increase in the boundary work is expected from Eq. (18): immediately after a shear reversal, frictional dissipation is negligible, the strain energy decreases and so the boundary work must decrease to maintain the energy balance. Once frictional dissipation resumes following a shear reversal, the boundary work increases once more. The kinetic energy has been omitted from Fig. 3(b), and all subsequent energy figures, because it is negligible: < 0.1% of the boundary work.

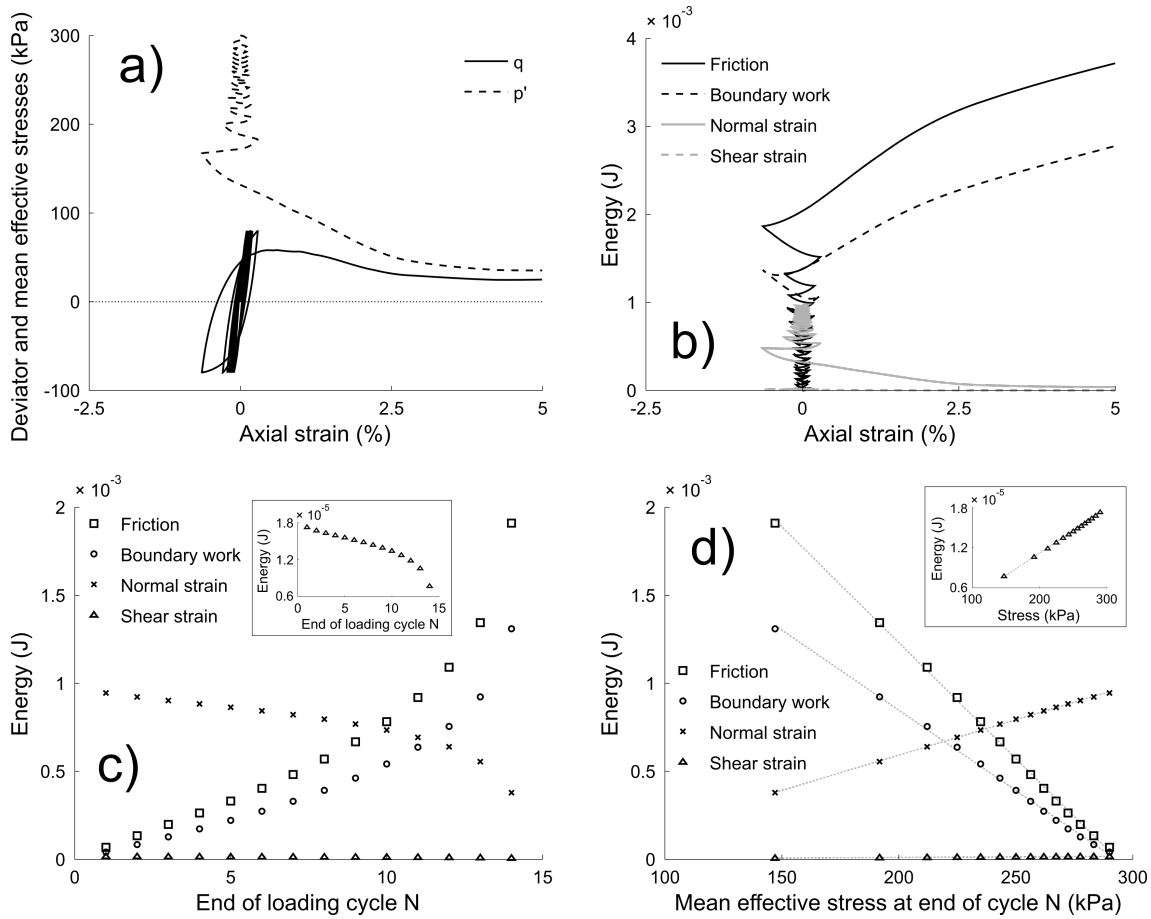

Fig. 3: Stress–strain behaviour and energy terms for S1 (base case) with e = 0.4534, p_0' = 300 kPa, q_{mean} = 0 kPa and q_{cyc} = 80 kPa: (a) deviator stress, q, and mean effective stress, p', against axial strain (%); (b) energy dissipated by frictional sliding, boundary work, and normal and shear components of strain energy, all in J, against axial strain; (c) values of these four energy terms at the end of loading cycle N against N; (d) the same values plotted against p' (kPa) where the dotted grey lines are linear regressions. The inset plots on (c) and (d) show data for the shear component of strain energy with reduced energy axes

The frictional dissipation and boundary work are almost equal for monotonic loading because the strain energy becomes negligible relative to the boundary work at large strains [13]. For cyclic loading, this is clearly not the case. The largest normal strain energy, at the start of shearing, is around one-third of the largest boundary work (at the onset of liquefaction). The boundary work is much less than in a monotonic simulation sheared to critical state because the strains, presented later in Fig. 12, are comparatively small.

The onset of liquefaction occurs during the 15th load cycle. Fig. 3(c) shows values of the four key energy terms at the end of each of the 14 preceding load cycles, N. The change in each energy term is nearly constant from cycle to cycle up to the 10th cycle, after which the rate of change increases. Fig. 3(d) plots the same data against p' rather than N. The dotted regression lines in Fig. 3(d) show that there are linear trends for all four energy terms ($R^2 > 0.998$) up to the onset of liquefaction.

4.2 Parametric study

Consider firstly the effect of sample void ratio on the various traced energy terms (Fig. 4). Although the range of void ratios considered is small, there are substantial differences in the number of complete cycles until the onset of liquefaction, N_l: 49, 14 and 4 for e = 0.4470, 0.4534 and 0.4586, respectively. $p' \approx 0$ kPa for both the densest (S2) and loosest (S3) samples at the onset of liquefaction. As the void ratio increases, the unit energy dissipated (energy dissipated per unit volume) up to the onset of liquefaction, δW_d, decreases from 8 kJ/m^3 (equivalent to 5.8 mJ) at e = 0.4470 to 4.5 kJ/m^3 (3.3 mJ) at e = 0.4586. For these simulations, recall that frictional sliding is the only energy dissipation mechanism. El Shamy & Denissen [20] observed that a 1% decrease in porosity caused an increase of around one order of magnitude in the energy dissipated at liquefaction. We capture the same trend but with much less sensitivity, more in line with experimental results, e.g., [5, 37]. Fig. 4(c) shows the non-monotonic decrease in strain energy that takes place during cycling. As for the boundary work, the normal strain energy increases approaching a shear reversal, and thereafter decreases sharply due to the sharp change in p' seen on Fig. 4(a). This makes sense from a consideration of the particle-scale micromechanics. Upon shear reversal, the strong force chains within the sample that bear the compressive load must reconfigure to accommodate the sudden change in loading direction. This leads to a temporary reduction in the heterogeneity of the contact force network and a corresponding sharp drop in strain energy. Once a new strong force network has been established, the strain energy can increase once again. Linear trends are again apparent in Fig. 4(d), although a slight curvature is noticeable for S2 with e = 0.4470.

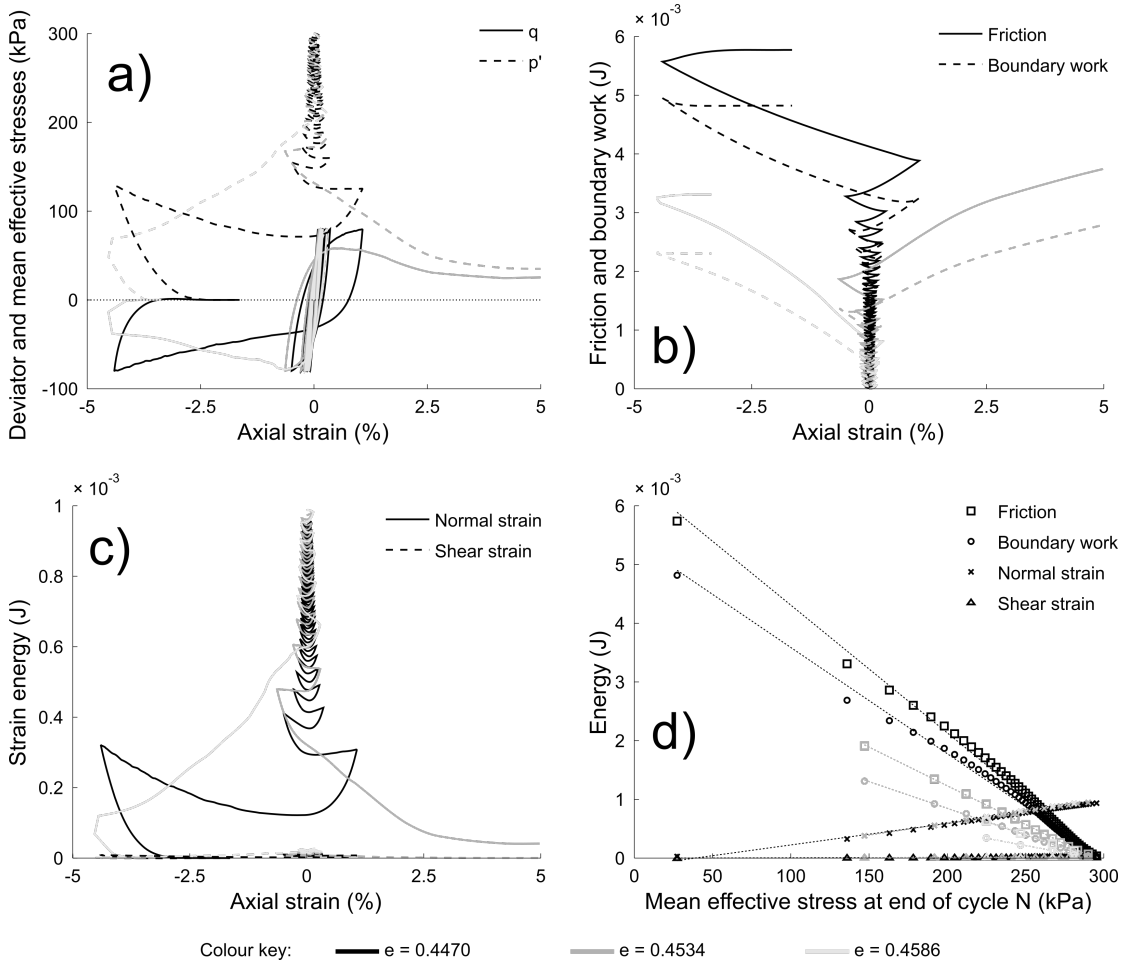

Fig. 4: Stress–strain behaviour and energy terms for the parametric study of void ratio where e = 0.4470 (S2), e = 0.4534 (S1) and e = 0.4586 (S3) are respectively represented by black, dark grey and light grey colours: (a) deviator stress, q, and mean effective stress, p', against axial strain (%); (b) boundary work and energy dissipated by frictional sliding, both in J, against axial strain; c) normal and shear components of strain energy (J) against axial strain; d) values of the four tracked energy terms at the end of loading cycle N against p' (kPa), including dotted linear regressions

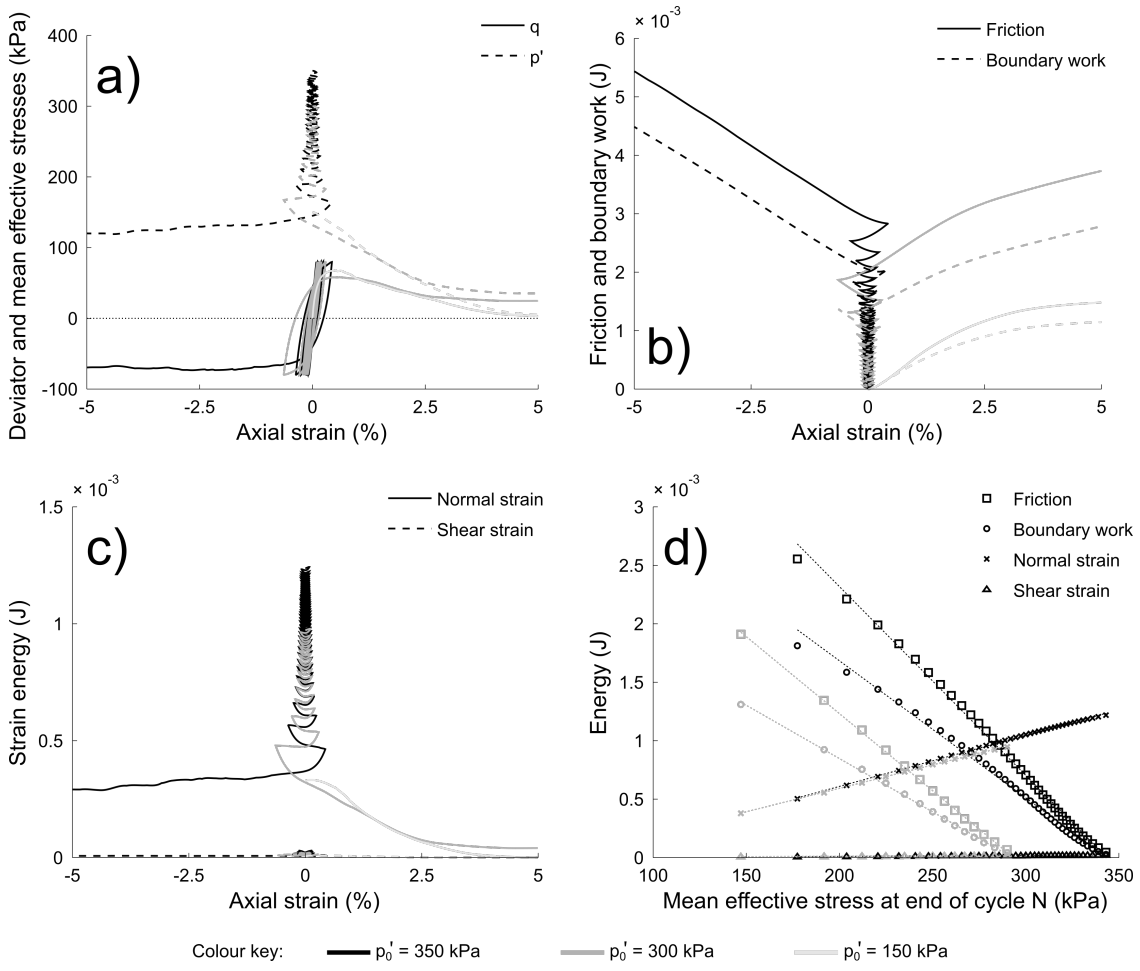

Fig. 5: Stress–strain behaviour and energy terms for the parametric study of initial mean effective stress where p_0' = 350 kPa (S4), p_0' = 300 kPa (S1) and p_0' = 150 kPa (S5) are respectively represented by black, dark grey and light grey colours. The four subfigures are as described for Fig. 4

Fig. 5 shows the parametric study of initial mean effective stress, p_0'. All three samples showed flow liquefaction behaviour. N_l reduces with p_0': 37, 14 and 0 for p_0' = 350 kPa, 300 kPa and 150 kPa, respectively (sample S5 with p_0' = 150 kPa liquefied during the first cycle). This can be partially attributed to the small changes of e, i.e., the p_0' = 350 kPa sample (S4) is the densest of these three while S5 is the loosest, but p_0' is influential regardless. δW_d decreases from 7.6 kJ/m^3 (5.5 mJ) to 2.0 kJ/m^3 (1.5 mJ) as p_0' decreases from 350 kPa to 150 kPa. The nearly linear decrease with p_0' matches experimental findings [38]. Based on an experimental testing programme using a hollow cylinder

apparatus, it was also found that increasing the effective confining pressure or relative density, i.e., increasing p'_0 or reducing e, increased δW_d [5, 10].

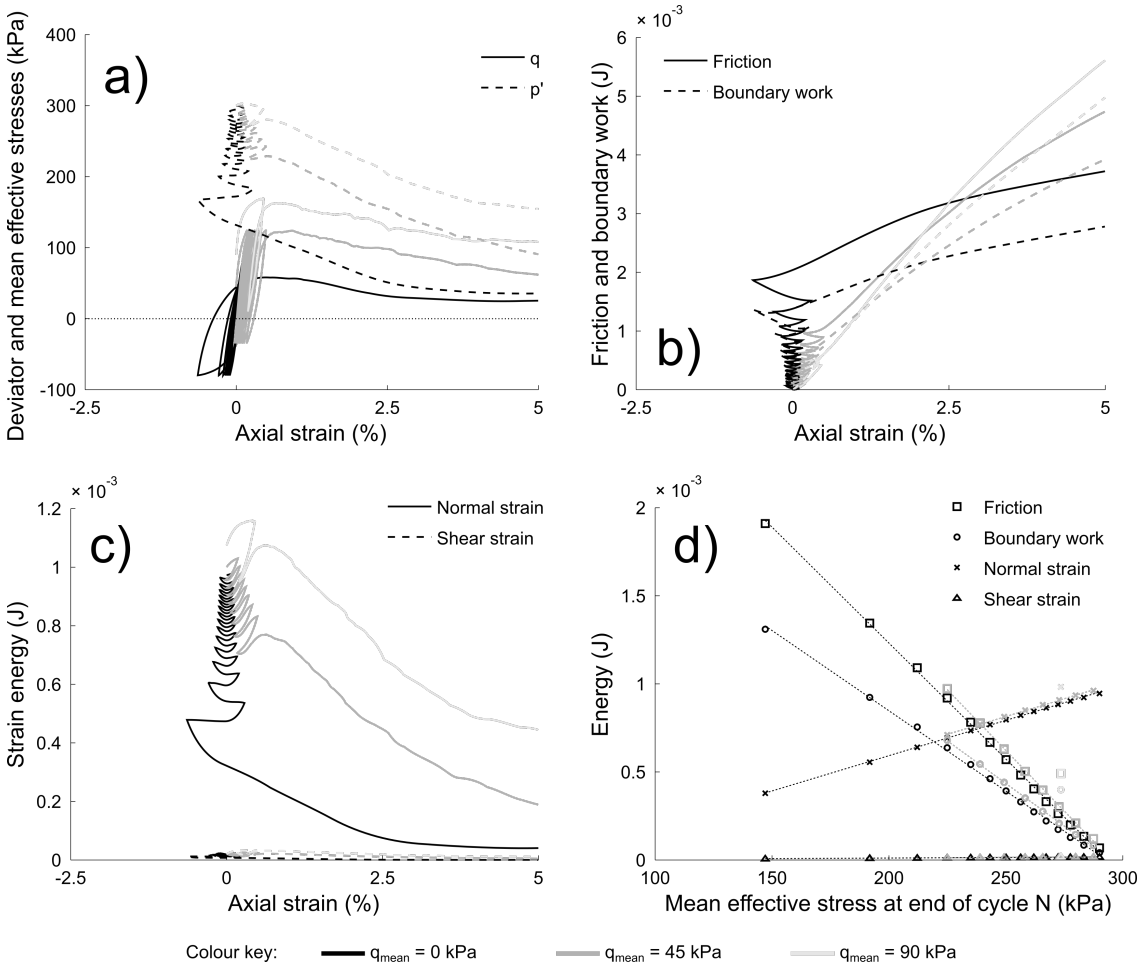

Fig. 6: Stress–strain behaviour and energy terms for the parametric study of mean deviator stress where q_{mean} = 0 kPa (S1), q_{mean} = 45 kPa (S6) and q_{mean} = 90 kPa (S7) are respectively represented by black, dark grey and light grey colours. The four subfigures are as described for Fig. 4

Fig. 6 compares the base case, S1, with two initially anisotropic samples (S6 and S7). By increasing the initial stress anisotropy, N_l reduces from 14 (isotropic) to 1 (S7 with q_{mean} = 90 kPa) even though both anisotropic samples are slightly denser than the isotropic one. As the anisotropic stress ratio $K_c = \sigma'_{z,0}/\sigma'_{x,0}$ increases, the cyclic stress path reaches the static failure envelope (instability line) sooner [39]. These three simulations, S1, S6 and S7, have K_c values of 1.0, 1.16 and 1.33,

respectively. The reduction in N_l caused by initial stress anisotropy does not lead to a commensurate reduction in the energy dissipated by friction: 3.8 mJ, 4.9 mJ and 5.8 mJ for q_{mean} = 0 kPa, 45 kPa and 90 kPa, respectively. This is the opposite of the behaviour seen in both Fig. 4 and Fig. 5 where a reduction in N_l, caused by either increasing e or reducing p'_0, was associated with a decrease in δW_d.

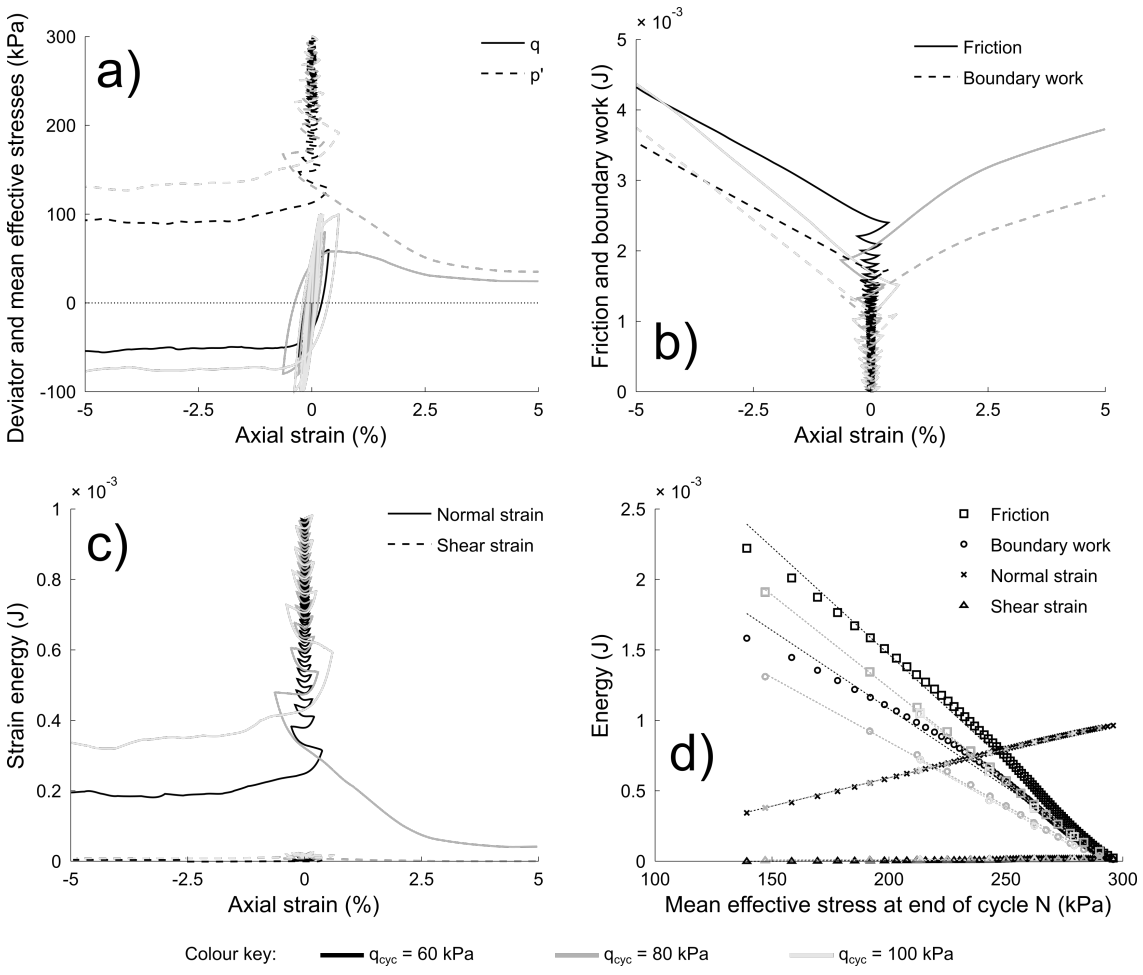

Fig. 7: Stress–strain behaviour and energy terms for the parametric study of deviator stress amplitude where q_{cyc} = 60 kPa (S8), q_{cyc} = 80 kPa (S1) and q_{cyc} = 100 kPa (S9) are respectively represented by black, dark grey and light grey colours. The four subfigures are as described for Fig. 4

Fig. 7 shows that increasing q_{cyc} reduces N_l from 69 at q_{cyc} = 60 kPa to 4 at q_{cyc} = 100 kPa. No significant effect was observed on δW_d, a result supported by laboratory experiments: Figueroa et al.

[5] found no clear relationship between δW_d and the shear strain amplitude, while Baziar & Sharafi [38] found no dependence on the cyclic stress ratio. This differs from a previous DEM study [20] which found that the energy dissipation increases substantially in line with the shear strain amplitude. More energy dissipation must occur during each load cycle as q_{cyc} increases in order for δW_d to remain unchanged as N_l reduces.

The final comparison in this parametric study was between the equivalent initial compression (S1) and initial extension (S10) cases. These were similar with N_l = 14 for both simulations. This may be because the sample was in an idealised isotropic state before cyclic shearing. It is possible that some differences in N_l would be observed for samples with initial anisotropy; however, it is outside the scope of this study which varies only a single parameter at a time from the base case values. The only noticeable difference was in δW_d: 5.3 kJ/m^3 (3.8 mJ) for S1 compared to 6.0 kJ/m^3 (4.4 mJ) for S10.

4.3 Inter- and intra-cycle variations in energy

This subsection focuses on the differences between cycles and within individual cycles of the base case simulation, S1. The rose diagrams in Fig. 8 show the frictional dissipation within three individual cycles: cycle 2 shortly after the start of cycling, cycle 8 in the middle of cycling, and cycle 14 which is the last complete cycle before the onset of liquefaction. The rose diagrams are drawn based on the spatial orientation of the branch vectors joining the centres of contacting spheres. In each rose diagram, the length of each segment is proportional to the total frictional dissipation that has occurred during that cycle for contacts with that particular branch vector orientation. The colours of the segments give a numerical indication of the frictional dissipation. 18 angular increments of 10° were considered between 0° and 180° in each Cartesian plane (*x*–*y*, *x*–*z* and *y*–*z*).

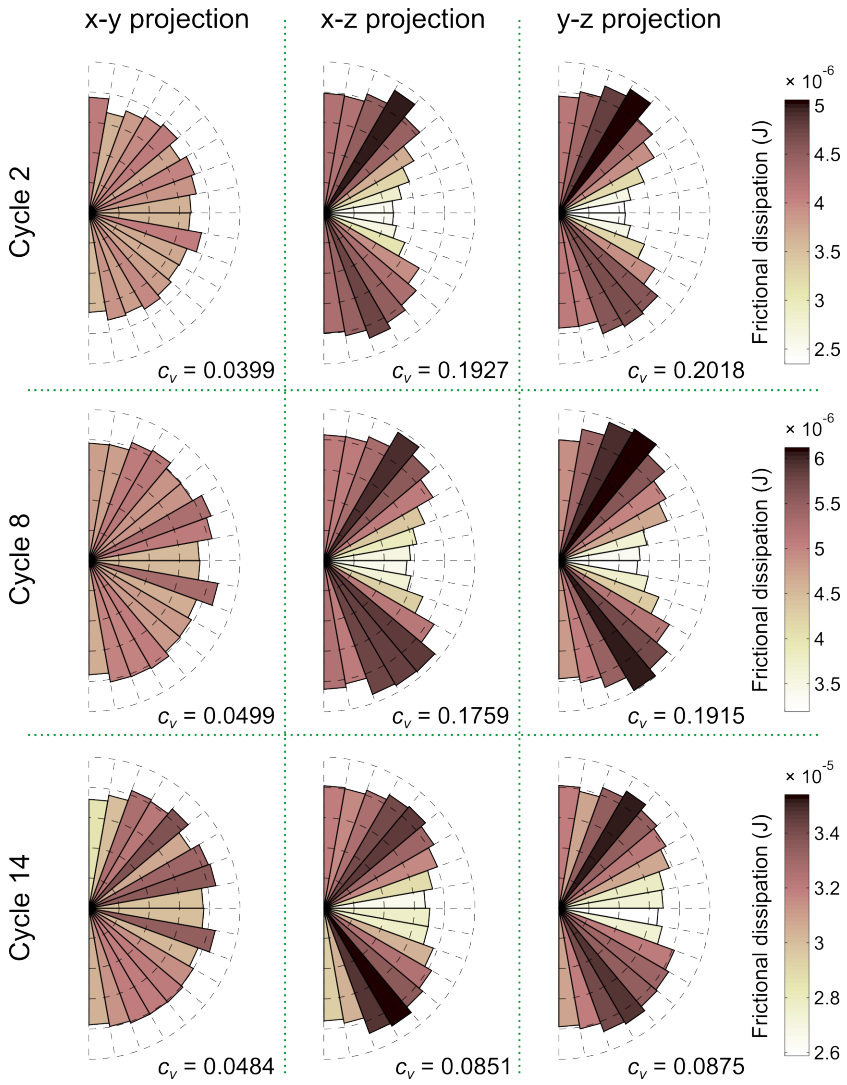

Fig. 8: Rose diagrams showing the total frictional dissipation (J) at each orientation for specific cycles of the base case simulation, S1. The three rows represent the dissipation during the 2nd (top), 8th (middle) and 14th (bottom) loading cycles. The three columns, from left to right, show projections onto the *x*–*y*, *x*–*z* and *y*–*z* planes. The lengths and colours of each segment show the total frictional dissipation for contacts at that orientation during the specified cycle

For all three cycles considered, frictional dissipation is isotropic for the horizontal *x*–*y* planes. In the vertical direction (*x*–*z* and *y*–*z* planes), more frictional dissipation takes place for contacts oriented between 30° and 40° than for any other orientation. This is reduced from the 40–50° preferred contact orientation for the monotonic simulations presented by [13]. Horizontally oriented contacts are associated with least energy dissipation, as in the monotonic simulations. The *x*–*z* and *y*–*z* rose

diagrams also show a systematic variation as cycling proceeds. Cycle 2 has the greatest variation between rose diagram segments while cycle 14 has the least. The heterogeneity of the energy dissipation can be quantified by computing the coefficient of variation, c_v, i.e., the standard deviation divided by the mean, of the 18 friction values shown on each rose diagram. Cycle 2 has a c_v of around 0.2 for the *x*–*z* and *y*–*z* planes: similar to the c_v at critical state for the monotonic simulations of Hanley et al. [13]. Since S1 is isotropic with $c_v \approx 0$ before cycling begins, this significant heterogeneity in the preferred orientation of frictional dissipation must develop rapidly upon shearing. Cycle 8 has a fractionally lower c_v than cycle 2, but c_v has diminished to around 0.09 by cycle 14: less than half of its value at cycle 2. Note also the different scales on the three colourbars. The friction dissipated during cycle 14 is nearly an order of magnitude greater than during cycle 2.

In addition to these differences between load cycles, there are also differences within a single cycle. Fig. 9 shows how the frictional dissipation, boundary work and strain energy vary with each individual cycle. Each cycle can be divided into quarters. For S1, loading is compressive from 0–0.25 and 0.75–1 cycles, and extensive from 0.25–0.75 cycles. Shear reversals occur at 0.25 and 0.75 cycles. The horizontal regions in Fig. 9(a) show negligible frictional dissipation immediately following a shear reversal. These 'zero friction' regions extend for around 0.04% axial strain. Beyond this threshold, the frictional dissipation grows quadratically ($R^2 > 0.99$). This indicates that, provided the applied load cycles have a sufficiently small amplitude, negligible frictional dissipation will occur. This explains why so many load cycles are needed to reach liquefaction if their amplitude is very small: N_l must be very large to accrue sufficient δW_d, which has no dependence on q_{cyc}, to induce liquefaction. The spacing between lines for $N - 1$ and N grows increasingly rapidly as the onset of liquefaction is approached. The quadratic growth in friction implies that most frictional dissipation ought to occur towards the end of the compressive or extensive loading phases. This is exactly what is observed: the energy dissipation during the half-cycle 0–0.25 & 0.5–0.75 is around one order of magnitude greater than during the other half-cycle.

The energy balance constrains Fig. 9(b) to have a similar appearance to Fig. 9(a). One interesting difference is that the boundary work decreases during the entire half-cycle 0.25–0.5 & 0.75–1 (post-

shear reversal when the magnitudes of the deviator stress and strain are decreasing); work input is needed solely for the other half-cycle. The normal component of strain energy decreases nonlinearly during a cycle (Fig. 9(c)). Its behaviour is completely different from the shear component (Fig. 9(d)) for which there are prominent local maxima at the shear reversals. This mirrors $|q|$: for S1, $|q|$ = 80 kPa at the shear reversals compared to $|q|$ = 0 kPa at 0 and 0.5 fractional cycles.

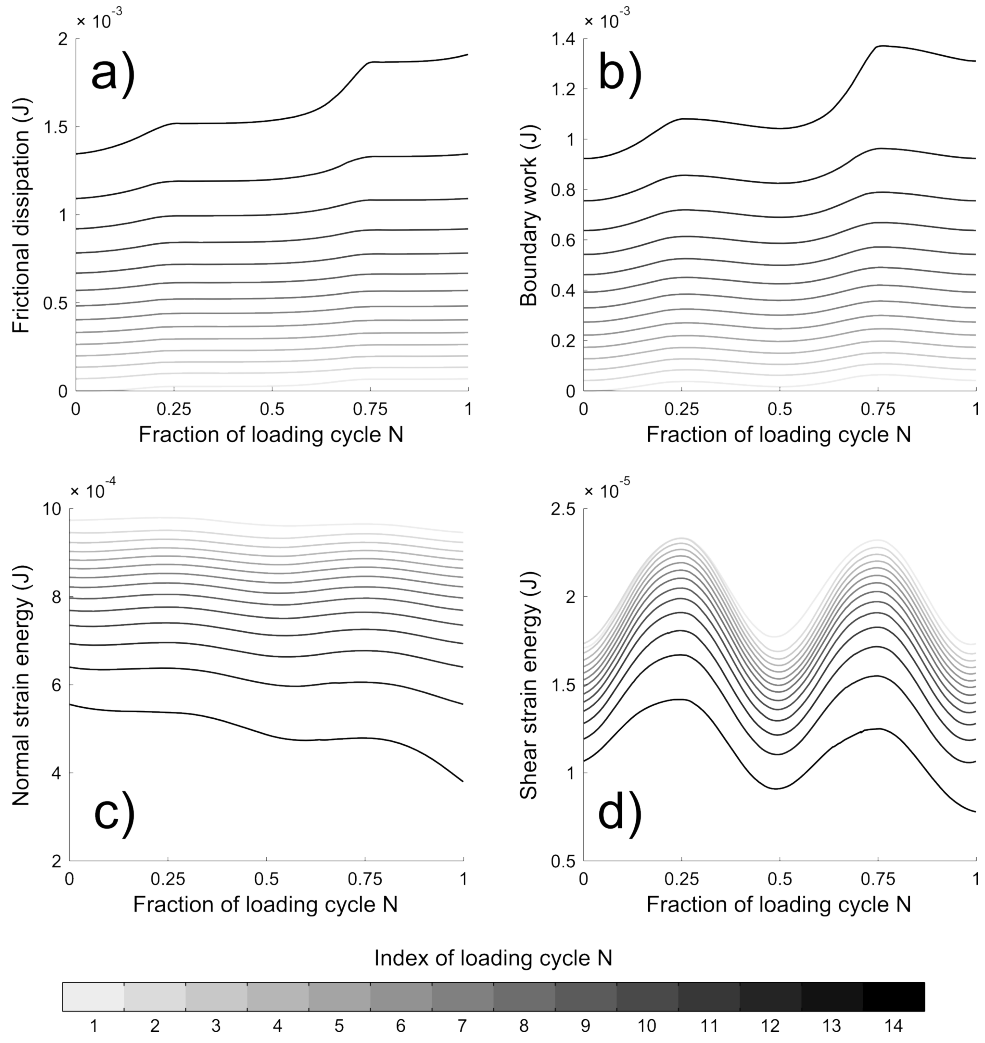

Fig. 9: Energy dissipated by frictional sliding (a), boundary work (b), normal (c) and shear (d) components of strain energy, all in J, against the fraction of loading cycle N for the base case simulation, S1. Individual cycles are distinguishable by colour, varying from light grey (1st cycle) to black (14th and final cycle before liquefaction) as indicated by the colourbar

The total frictional dissipation for cycle 8 of S1 is given in Fig. 8; Fig. 10 shows the analogous rose diagram projections onto the *y*–*z* plane for the individual quarter-cycles 7–7.25, 7.25–7.5, 7.5–7.75 and 7.75–8. Although there are seemingly minor differences between these four diagrams, the coefficients of variation reveal a greater heterogeneity in the orientations of contacting particles at which frictional dissipation occurs for the extensive half-cycle than the compressive half-cycle. Apart from confirming that c_v declines during shearing, Fig. 11 also shows that extension leads to a higher c_v than compression throughout the simulation, regardless of whether the first quarter-cycle is compressive (Fig. 11(a)) or extensive (Fig. 11(b)). Considering Fig. 12, compression, in which one boundary (z in this case) moves inwards and the two lateral boundaries outwards, leads to a more homogeneous pattern of frictional dissipation than extension, in which one boundary moves outwards and two inwards. This is a very interesting observation. The trend is unrelated to the magnitude of the frictional dissipation (Fig. 9(a)): dissipation is negligible immediately following a shear reversal regardless of compressive or extensive loading. It is also unrelated to the second-order fabric tensor, Φ_{pq}, which is a useful measure of fabric anisotropy [40]:

$$\Phi_{pq} = \sum_{j=1}^{N_c} \boldsymbol{n_p^j n_q^j} \tag{19}$$

where $\boldsymbol{n}_p^j$ is the unit contact normal for contact j. The difference between the maximum and minimum eigenvalues of the Φ_{pq} tensor is termed the deviatoric fabric. Fig. 13(a) shows the variation of deviatoric fabric with N for S1. The cyclic trends in deviatoric fabric are linked to trends in q and match the trends in frictional dissipation: increasing deviatoric fabric is associated with increasing $|q - q_{mean}|$ and those quarter-cycles with high frictional dissipation. Conversely, decreasing deviatoric fabric is linked to low dissipation and decreasing $|q - q_{mean}|$. The same observation is true for other simulations such as S6 with initial stress anisotropy (Fig. 13(b)). Comparing Fig. 11 and Fig. 13 shows that even though the fabric becomes increasingly anisotropic as cycling proceeds, the anisotropy in the pattern of energy dissipation becomes less pronounced.

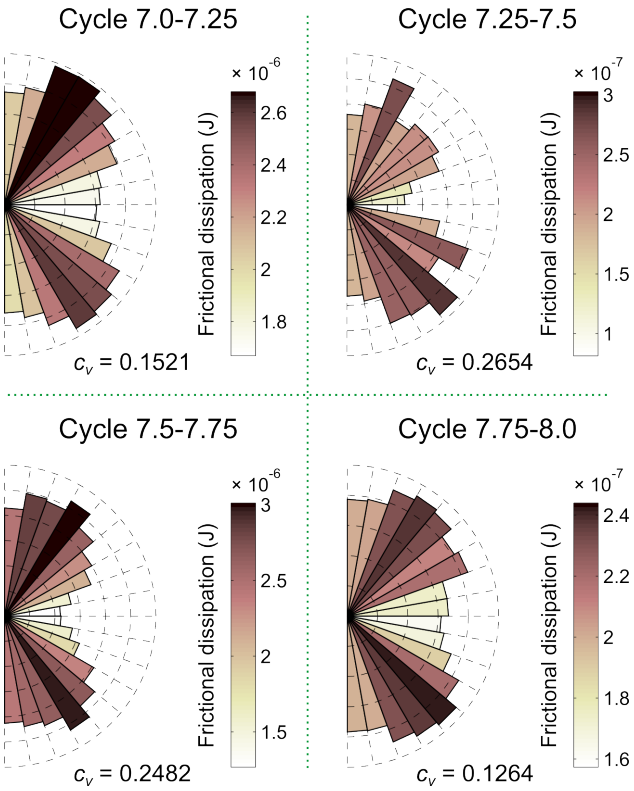

Fig. 10: Rose diagrams showing the total frictional dissipation (J) at each orientation for four consecutive quarter-cycles comprising one complete loading cycle of the base case simulation, S1. The frictional dissipation is shown for cycle 8, i.e., the middle row of Fig. 8. Each diagram shows a projection onto the *y*–*z* plane

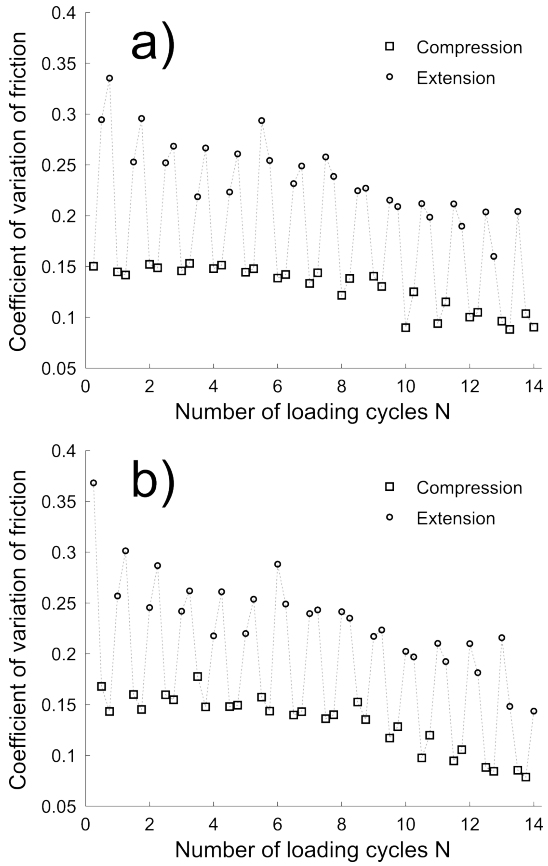

Fig. 11: Coefficient of variation among the 36 bins for total frictional dissipation for projections onto the *x*–*z* and *y*–*z* planes against the number of loading cycles *N*. (a) is for the base case IC simulation, S1; (b) is for the IE simulation, S10. Each data point is based on a quarter-cycle, as for the rose diagrams in Fig. 10. Markers distinguish compressive (□) from extensive (o) loading; the grey dotted lines are a visual aid

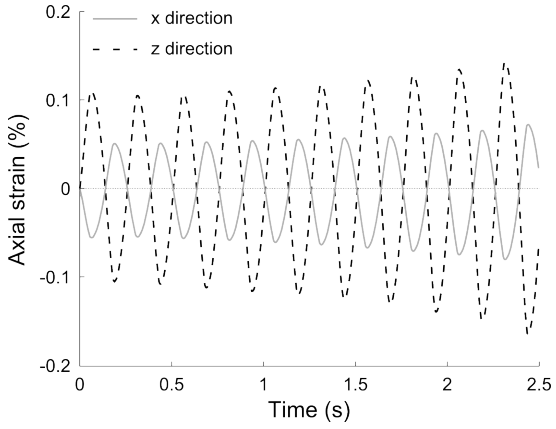

Fig. 12: Percentage axial strains against time for the initial cycles of S1

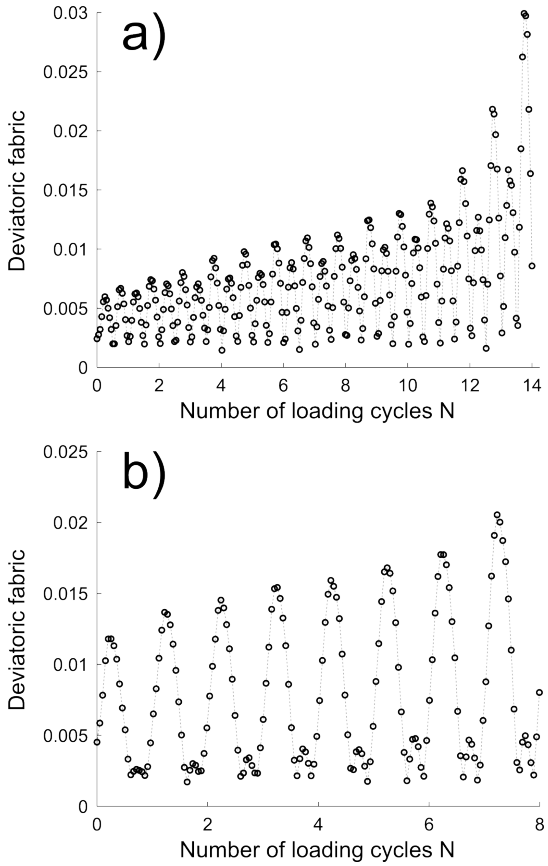

Fig. 13: Deviatoric fabric of all contacts against the number of loading cycles N for (a) the base case simulation, S1 and (b) the q_{mean} = 45 kPa simulation, S6. The grey dotted lines are a visual aid

4.4 Relationship between stress and energy

The relationship between the accumulated pore water pressure increase and the dissipated energy per unit volume during undrained cyclic loading has been investigated experimentally [4, 9, 37, 38, 41-43]. Some authors have reported a unique relationship for a given soil type, after normalisation by the initial confining pressure when necessary; others have found a dependence on the specimen density [41] or the cyclic deviator stress [43].

The dissipated energy is readily and precisely available from DEM; it does not require estimation from the areas of stress–strain hysteresis loops. Fig. 14 shows the normalised data for all 10

simulations. Δu was computed for these constant-volume simulations as $\sigma'_x - \sigma'_{x,0}$ (equivalent to $p'_0 - p'$ since q is prescribed by Eq. (1)). All plots have a similar trend and alignment. The data for the lowest and highest void ratios bound the other data. e is clearly the most influential factor, despite its small variation in these simulations: as e increases from 0.4470 to 0.4586, there is a noticeable upward shift on Fig. 14. This is in agreement with experimental data [41]. Apart from e, none of the other factors explored in the parametric study significantly affect the relationship between the pore water pressure and unit energy.

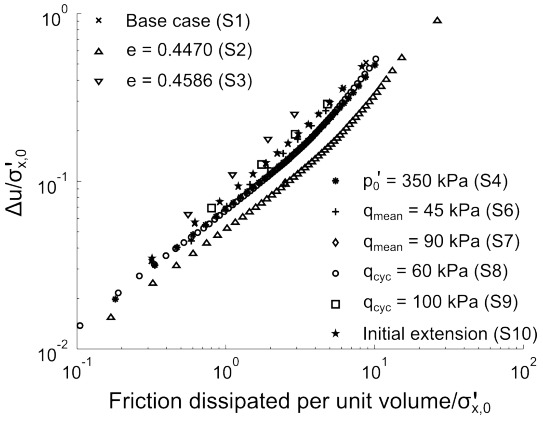

Fig. 14: Accumulated pore water pressure increase normalised by initial confining pressure, $\sigma'_{x,0}$, against the accumulated friction dissipated per unit volume (unit energy) with the same normalisation. The markers show values at the end of each complete loading cycle

The energy dissipated during a single cycle is plotted against the change in p' during that cycle in Fig. 15. A bilinear trend emerges which is most obvious for those simulations with large N_l. During the initial cycles, the particles reorganise so as to bear the applied load. Both the frictional dissipation and change in $|p'|$ per cycle decrease until a minimum is reached. There can then be many cycles in which the changes which occur are almost imperceptible. However, the mechanical coordination number [44] and indices of redundancy [45, 46] gradually decrease with each cycle until eventually the

frictional dissipation and change in $|p'|$ per cycle begin to increase. The rate of increase accelerates until the onset of liquefaction. The decreasing and increasing trends have distinct slopes.

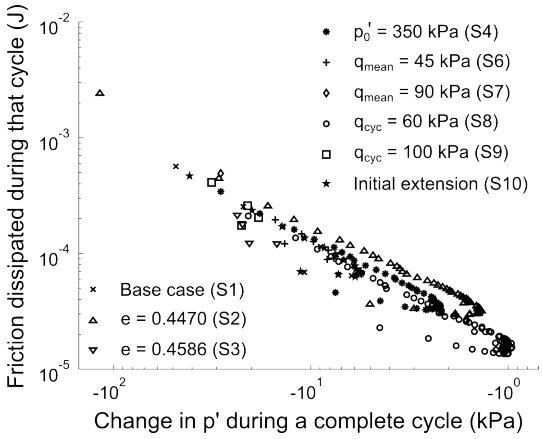

Fig. 15: Friction dissipated during a single loading cycle (J) against the change in mean effective stress, p', during that cycle (kPa)

4.5 Energy-based models for liquefaction assessment

Many models have been proposed to evaluate the liquefaction potential of soils based on dissipated energy [8]. These models have been derived from experimental data for various sands. Most are a function only of initial effective confining pressure and initial relative density; the model proposed by [47] also takes the soil grading into account. In this paper, we focus on the popular model proposed by Figueroa et al. [5] which is conveniently expressed in terms of effective confining pressure (in kPa) and e rather than relative density:

$$\log_{10} \delta W_d = a + b\sigma'_{x,0} - ce \tag{20}$$

a, b, c are constants, and δW_d, the unit energy up to the onset of liquefaction, is in J/m^3. The values obtained for these constants, based on 27 laboratory tests of Reid Bedford sand, are given in Table 2 [5]. Fitting Eq. (20) with these constants to the DEM data led to large over-predictions of δW_d by factors between 10 and 35 and an adjusted R^2 of 0.2621. Such a poor fit is unsurprising: our

simulations of perfectly smooth spheres do not permit plastic deformation, asperity crushing or grain breakage. The simulations also do not capture any energy dissipation due to the fluid phase which is present in the experiments. At least some of the disparity may be attributed to these omissions. A new set of constants, also given in Table 2, was obtained through best-fitting Eq. (20) to the simulation data. This improved the adjusted R^2 to 0.7757: reasonable agreement considering the simplicity of the model. Fig. 16(a) compares the predicted and actual δW_d values. S6 and S7, the two samples with initial stress anisotropy, are the principal outliers. Eq. (20) does not take q_{mean} into consideration; this was not one of the factors considered by Figueroa et al. [5] and later models have also ignored this factor [8]. Consider Eq. (21) which includes q_{mean} (kPa):

$$\log_{10} \delta W_d = a + b\sigma'_{x,0} - ce + \mathrm{d}q_{mean} \tag{21}$$

The inclusion of q_{mean} improves the adjusted R^2 to 0.97 and brings the δW_d values for S6 and S7 into line with the data for the initially isotropic samples, as shown in Fig. 16(b). If an energy-based model is being applied for liquefaction assessment of anisotropic samples, a significant improvement in the accuracy of the model may be achieved by including the mean deviator stress.

Table 2. Constants in Eq. (20) and (21) for Reid Bedford sand [5] and model fitting using the simulation data reported in this paper, along with adjusted R^2 statistics for these models

Source	a	b	c	d	Adjusted R^2
Figueroa et al. [5]	5.697	0.00477	4.339	–	0.2621
Best-fit of Eq. (20)	13.815	0.00128	22.981	–	0.7757
Best-fit of Eq. (21)	12.852	0.00164	21.120	0.00156	0.9700

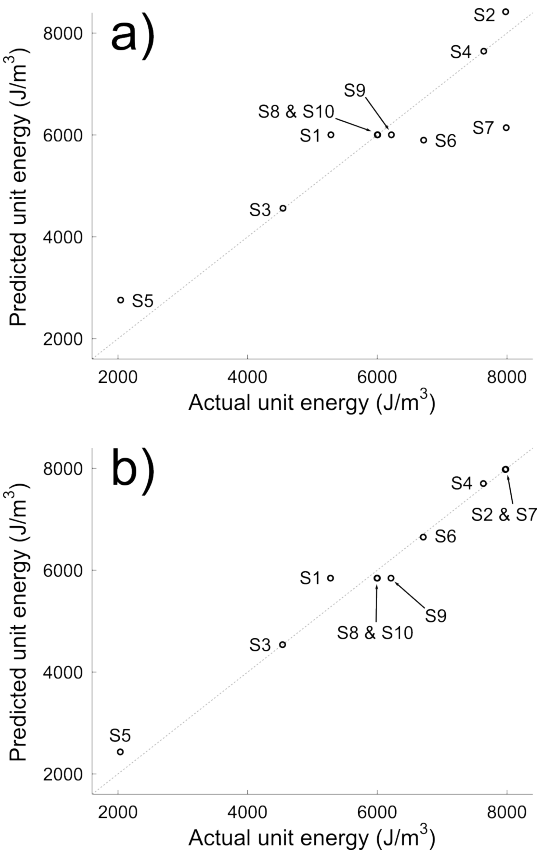

Fig. 16: Comparison between the total frictional dissipation per unit volume, i.e., unit energy, at the onset of liquefaction (J/m^3) for the ten simulations described in this paper and the predictions made using (a) Eq. (20); (b) Eq. (21)

5 Conclusions

A set of 10 constant-volume cyclic triaxial simulations with energy tracing active have been conducted in accordance with a parametric study of five factors: void ratio, initial mean effective stress, mean deviator stress, deviator stress amplitude and compressive/extensive initial loading. By increasing the void ratio or decreasing the initial mean effective stress, both the number of complete cycles and the energy dissipated per unit volume up to the onset of liquefaction, respectively denoted as N_l and δW_d, are reduced. Void ratio is the only factor from those investigated which significantly affects the relationship between the excess pore water pressure and δW_d. Initial stress anisotropy reduces N_l but increases δW_d. Increasing the deviator stress amplitude also reduces N_l but this

parameter has no significant effect on δW_d. All of these observed trends in N_l and δW_d match data from physical experiments, where available.

The preferred contact orientation for frictional dissipation is between 30° and 40° for these cyclic simulations: lower than for the drained monotonic simulations described by [13]. Horizontally oriented contacts are associated with least energy dissipation. A significant heterogeneity in the preferred orientation of frictional dissipation develops rapidly upon shearing; this heterogeneity declines nonlinearly as cycling proceeds. There is a greater heterogeneity for extension than for compression, regardless of whether the initial phase of loading is compressive or extensive. Immediately following a shear reversal, the boundary work decreases and there is a period of negligible frictional dissipation which lasts for around 0.04% axial strain. Thereafter, the frictional dissipation grows quadratically, i.e., most frictional dissipation occurs towards the end of the compressive or extensive loading phases. This explains why so many load cycles are needed to reach liquefaction if their amplitude is very small: load cycles with amplitudes less than a particular threshold (0.04% axial strain for these simulations) cause negligible frictional dissipation. N_l must therefore be very large to accrue sufficient δW_d to induce liquefaction.

The model proposed by [5] to evaluate the liquefaction potential of a soil gives reasonable agreement for these data using best-fit parameters (adjusted R^2 of 0.7757). However, the inclusion of mean deviator stress, a factor omitted from all commonly used models of this type [8], significantly improves the adjusted R^2 to 0.97. This inclusion is strongly recommended to improve the predictive ability for samples with initial stress anisotropy.

Acknowledgements

This work used the ARCHER UK National Supercomputing Service (http://www.archer.ac.uk). The second author acknowledges the financial support of the National Natural Science Foundation of China (No. 51509186).

Appendix A

As described in Section 2, some researchers [33] have recommended rescaling the value of shear force carried forward from the previous time-step whenever the normal force decreases, prior to updating the shear force using Eq. (3). However, this rescaling leads to an overestimation of the energy dissipated [34], i.e., an unexplained loss of energy from the system.

Consider a collision of two identical particles, A and B, of diameter 1 cm and density 2670 kg/m^3. A is initially located at the origin while B is located a distance of 0.0101 m along the x-axis, i.e., their initial separation is 100 μm. A is given an initial translational velocity of [6, 3, 0] m/s (x, y, z components of velocity, respectively). B's translational velocity is initialised at [0, 0, 3] m/s and in addition B is assigned an initial rotational velocity of [0, 0, -3] rad/s. Two simulations were run with a simplified Hertz-Mindlin contact model, G = 2 MPa, υ = 0.2, μ = 0.25 and a very conservative time-step of 10 ns. The only difference between the simulations is the inclusion or omission of the shear force rescaling [33]. Each simulation was run for 1 ms, i.e., 100,000 timesteps, by which time the particles had collided and fully separated.

Fig. A1(a) shows that the energy terms appear similar regardless of whether the shear force has been rescaled or not. The kinetic energy and frictional dissipation are both fractionally lower in the rescaled case. The total energy is the sum of frictional dissipation, kinetic and strain energy. This deviates from a horizontal line during the unloading phase of the collision, when the normal force decreases, for the rescaled case. This deviation indicates that energy is not properly conserved. The error in the energy balance is quantified as a percentage of the total energy in Fig. A1(b). At the end of the two simulations, the errors are < 2 x 10^{-6}% and 0.48% for the unscaled and rescaled cases, respectively. Over the course of a long simulation containing tens of thousands of particles and billions of time-steps, the accumulated error in the energy balance would be unacceptable if this rescaling were adopted.

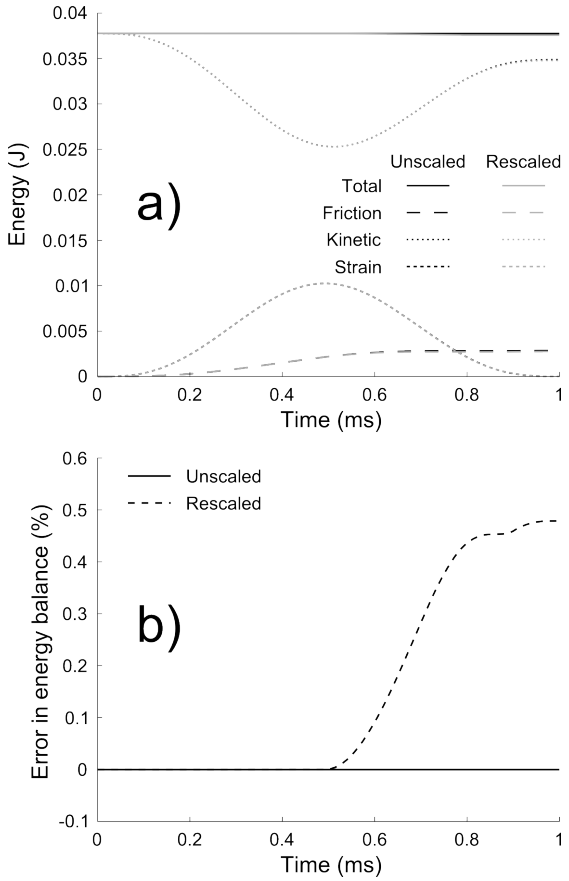

Fig. A1: (a) Friction dissipated, kinetic energy, strain energy and total energy in J against time in ms for a collision of two particles with and without the rescaling of old shear force; (b) comparison of the errors in the energy balance expressed as a percentage of the total energy

References

[1] Seed, H. B., Wong, R. T., Idriss, I. M. & Tokimatsu, K. (1986). Moduli and damping factors for dynamic analyses of cohesionless soils. *J. Geotech. Eng*. **112**, No. 11, 1016–1032.

[2] Vucetic, M. & Dobry, R. (1991). Effect of soil plasticity on cyclic response. *J. Geotech. Eng*. **117**, No. 1, 89–107.

[3] Berrill, J. B. & Davis, R. O. (1985). Energy dissipation and seismic liquefaction of sands: revised model. *Soils Found*. **25**, No. 2, 106–118.

[4] Law, K. T., Cao, Y. L., & He, G. N. (1990). An energy approach for assessing seismic liquefaction potential. *Can. Geotech. J*. **27**, No. 3, 320–329.

[5] Figueroa, J. L., Saada, A. S., Liang, L. & Dahisaria, N. M. (1994). Evaluation of soil liquefaction by energy principles. *J. Geotech. Eng*. **120**, No. 9, 1554–1569.

[6] Trifunac, M. D. (1995). Empirical criteria for liquefaction in sands via standard penetration tests and seismic wave energy. *Soil Dyn. Earthq. Eng*. **14**, 419–426.

[7] Dief, H. M. & Figueroa, J. L. (2007). Liquefaction assessment by the unit energy concept through centrifuge and torsional shear tests. *Can. Geotech. J*. **44**, No. 11, 1286–1297.

[8] Alavi, A. H. & Gandomi, A. H. (2012). Energy-based numerical models for assessment of soil liquefaction. *Geosci. Front*. **3**, No. 4, 541–555.

[9] Kokusho, T. (2013). Liquefaction potential evaluations: energy-based method versus stress-based method. *Can. Geotech. J*. **50**, No. 10, 1088–1099.

[10] Liang, L., Figueroa, J. L. & Saada, A. S. (1995). Liquefaction under random loading: unit energy approach. *J. Geotech. Eng*. **121**, No. 11, 776–781.

[11] Seed, H. B & Idriss, I. M. (1971). Simplified procedure for evaluating soil liquefaction potential. *J. Soil Mech. Found. Div*. **97**, No. 9, 1249–1273.

[12] Dobry, R., Ladd, R. S., Yokel, F. Y., Chung, R. M. & Powell, D. (1982). *Prediction of pore water pressure build-up and liquefaction of sands during earthquakes by the cyclic strain method*. National Bureau of Standards Building Science Series 138. Washington: US Government Printing Office.

[13] Hanley, K. J., Huang, X. & O'Sullivan, C. (2018). Energy dissipation in soil samples during drained triaxial shearing. *Géotechnique* **68**, No. 5, 421–433.

[14] Cheng, Y. P., Bolton, M. D. & Nakata, Y. (2004). Crushing and plastic deformation of soils simulated using DEM. *Géotechnique* **54**, No. 2, 131–141.

[15] Bolton, M. D., Nakata, Y. & Cheng, Y. P. (2008). Micro- and macro-mechanical behaviour of DEM crushable materials. *Géotechnique* **58**, No. 6, 471–480.

[16] Bi, Z., Sun, Q., Jin, F. & Zhang, M. (2011). Numerical study on energy transformation in granular matter under biaxial compression. *Granul. Matter* **13**, No. 4, 503–510.

[17] Wang, J. & Yan, Y. (2012). DEM analysis of energy dissipation in crushable soils. *Soils Found*. **52**, No. 4, 644–657.

[18] Zhang, W., Wang, J. & Jiang, M. (2013). DEM-aided discovery of the relationship between energy dissipation and shear band formation considering the effects of particle rolling resistance. *J. Geotech. Geoenviron*. **139**, No. 9, 1512–1527.

[19] El Shamy, U. & Denissen, C. (2010). Microscale characterization of energy dissipation mechanisms in liquefiable granular soils. *Comput. Geotech*. **37**, 846–857.

[20] El Shamy, U. & Denissen, C. (2012). Microscale energy dissipation mechanisms in cyclically-loaded granular soils. *Geotech. Geol. Eng*. **30**, No. 2, 343–361.

[21] Zamani, N. & El Shamy, U. (2013). Discrete-element method simulations of the response of soil-foundation-structure systems to multidirectional seismic motion. *Int. J. Geomech*. **13**, No. 5, 595–610.

[22] Tong, L. & Wang, Y. H. (2015). DEM simulations of shear modulus and damping ratio of sand with emphasis on the effects of particle number, particle shape, and aging. *Acta Geotech*. **10**, 117–130.

[23] Huang, X., Hanley, K. J., O'Sullivan, C. & Kwok, F. C. Y. (2014a). Effect of sample size on the response of DEM samples with a realistic grading. *Particuology* **15**, 107–115.

[24] Hanley, K. J., Huang, X., O'Sullivan, C. & Kwok, F. C. Y. (2014). Temporal variation of contact networks in granular materials. *Granul. Matter* **16**, No. 1, 41–54.

[25] Potyondy, D. O. & Cundall, P. A. (2004). A bonded-particle model for rock. *Int. J. Rock Mech. Min*. **41**, No. 8, 1329–1364.

[26] Huang, X., Hanley, K. J., O'Sullivan, C. & Kwok, C. Y. (2014b). Exploring the influence of interparticle friction on critical state behaviour using DEM. *Int. J. Numer. Anal. Met*. **38**, No. 12, 1276–1297.

[27] Salvati, L. A. & Anhdan, L. Q. (2008). Rate-dependent response of dense sand in cyclic triaxial tests. *Soils Found*. **48**, No. 3, 447–451.

[28] Airey, D. W. & Fahey, M. (1991). Cyclic response of calcareous soil from the North-West Shelf of Australia. *Géotechnique* **41**, No. 1, 101–121.

[29] Lopera Perez, J. C., Kwok, C. Y., O'Sullivan, C., Huang, X. & Hanley, K. J. (2016). Assessing the quasi-static conditions for shearing in granular media within the critical state soil mechanics framework. *Soils Found*. **56**, No. 1, 152–159.

[30] Ishihara, K. (1993). Liquefaction and flow failure during earthquakes. *Géotechnique* **43**, No. 3, 351–415.

[31] Yang, J. & Sze, H. Y. (2011). Cyclic behaviour and resistance of saturated sand under non-symmetrical loading conditions. *Géotechnique* **61**, No. 1, 59–73.

[32] Plimpton, S. (1995). Fast parallel algorithms for short-range molecular dynamics. *J. Comput. Phys*. **117**, 1–19.

[33] Thornton, C., Cummins, S. J. & Cleary, P. W. (2013). An investigation of the comparative behaviour of alternative contact force models during inelastic collisions. *Powder Technol*. **233**, 30–46.

[34] Elata, D. & Berryman, J. G. (1996). Contact force-displacement laws and the mechanical behavior of random packs of identical spheres. *Mech. Mater*. **24**, 229–240.

[35] Hanley, K. J., Huang, X., O'Sullivan, C. & Kwok, F. (2013). Challenges of simulating undrained tests using the constant volume method in DEM. *AIP Conf. Proc.* **1542**, 277–280.

[36] Muir Wood, D. (1990). *Soil behaviour and critical state soil mechanics*. Cambridge, UK: Cambridge University Press.

[37] Azeiteiro, R. J. N., Coelho, P. A. L. F., Taborda, D. M. G. & Grazina, J. C. D. (2017). Energy-based evaluation of liquefaction potential under non-uniform cyclic loading. *Soil Dyn. Earthq. Eng*. **92**, 650–665.

[38] Baziar, M. H. & Sharafi, H. (2011). Assessment of silty sand liquefaction potential using hollow torsional tests – An energy approach. *Soil Dyn. Earthq. Eng*. **31**, 857–865.

[39] Konrad, J.-M. (1993). Undrained response of loosely compacted sands during monotonic and cyclic compression tests. *Géotechnique* **43**, No. 1, 69–89.

[40] Satake, M. (1982). Fabric tensor in granular materials. In *Proceedings of the IUTAM symposium on deformations and failure of granular materials 1982* (eds P. A. Vermeer and H. J. Luger), pp. 63–68. Rotterdam, the Netherlands: Balkema.

[41] Okada, N. & Nemat-Nasser, S. (1994). Energy dissipation in inelastic flow of saturated cohesionless granular media. *Géotechnique* **44**, No. 1, 1–19.

[42] Towhata, I. & Ishihara, K. (1985). Shear work and pore water pressure in undrained shear. *Soils Found*. **25**, No. 3, 73–84.

[43] Simcock, K. J., Davis, R. O., Berrill, J. B. & Mullenger, G. (1983). Cyclic triaxial tests with continuous measurement of dissipated energy. *Geotech. Test. J*. **6**, No. 1, 35–39.

[44] Thornton, C. (2000). Numerical simulations of deviatoric shear deformation of granular media. *Géotechnique* **50**, No. 1, 43–53.

[45] Kruyt, N. P. & Rothenburg. L. (2009). Plasticity of granular materials: a structural-mechanics view. *AIP Conf. Proc*. **1073**, No. 1, 1073–1076.

[46] Huang, X., Kwok, C.-Y., Hanley, K. J. & Zhang, Z. (2018). DEM analysis of the onset of flow deformation of sands: linking monotonic and cyclic undrained behaviours. *Acta Geotech.* **13**, 1061–1074.

[47] Baziar, M. H. & Jafarian, Y. (2007). Assessment of liquefaction triggering using strain energy concept and ANN model: Capacity Energy. *Soil Dyn. Earthq. Eng*. **27**, 1056–1072.